Electronic Supplementary Material (ESI) for Journal of Materials Chemistry C.

A general strategy to immobilize metal nanoparticles on MXene composites fabric for enhanced sensing performance and endowed multifunctionality

Qinghua Yu [a,b], Junjie Pan [b,c], Jianna Li [b,c], Chuanli Su [b,c], Yaoli Huang [b,c], Siyi Bi [a,b]*, Jinhua Jiang [a,b]* and Nanliang Chen [a,c]

[a] Shanghai Frontier Science Research Center for Modern Textiles, Donghua University, Shanghai 201620, P. R. China

[b] Shanghai Collaborative Innovation Center of High Performance Fibers and Composites, College of Textiles, Donghua University, Shanghai, 201620, P. R. China

[c] Engineering Research Center of Technical Textiles, Ministry of Education, Donghua University, Shanghai, 201620, P. R. China

* Corresponding authors. E-mail addresses: siyibi@dhu.edu.cn (Siyi Bi), jiangjinhua@dhu.edu.cn (Jinhua Jiang).

Characterization

Morphology and structure. The morphologies of seven samples (Ti_3AlC_2, m-$Ti_3C_2T_x$, s-$Ti_3C_2T_x$, NWF, MNWF, AgNPs@MNWF and AuNPs@MNWF) were observed using field emission scanning electron microscopy (FE-SEM, JSM-7500F, China). The elemental distribution of the samples was confirmed using an energy spectrometer (EDS, SU8010). High-resolution transmission electron microscopy (HR-TEM, Talos F200S) and atomic force microscopy (AFM, NanoScope IV, U.S.A.) were used to observe further and measure the morphological structure and thickness dimensions s-$Ti_3C_2T_x$ nanosheets, respectively. The corresponding crystallinity characteristics of each sample were demonstrated by X-ray diffraction spectroscopy (XRD, Bruker D8 ADVANCE). The elemental composition and corresponding valence state of each sample were determined using X-ray photoelectron spectroscopy (XPS, */Escalab 250Xi). Fourier transform infrared spectroscopy (FTIR, */NEXUS-670) was used to study the interaction between the fabric and MXene. The structure and morphology of AuNPs were characterized and analyzed using aberration-corrected scanning transmission electron microscopy (aberration-corrected-STEM). The static contact angle of the NWF was measured by the Captive bubble method using an optical contact angle tester (OCA15EC). The content of MXene in MNWF composite fabrics was determined by an inductively coupled plasma optical emission spectrometer (ICP, Varian VISTA-157 MPX ICP-OES). The UV spectra of MXene solution, AuNPs@MXene heterojunction solution, and AgNPs@MXene heterojunction solution

were recorded by UV-Vis-NIR absorption spectrometer (UV3600). All-optical photos were taken with a mobile phone (MI 9).

Tensile properties and breathability. The tensile properties of the fabrics were tested using a universal material testing machine (CMT model E42, MTS) according to the standard GB/T 3923.1-2013. The air permeability of the fabric was obtained by using a fabric automatic air permeability tester (YG461E) according to the standard GB/T166 5453:1997.1.

Electrical and sensing properties. A multimeter (Keysight 34461A) was used to determine the resistance of the composite fabric and sensor. In this work, to test the sensing performance of the flexible pressure sensor, a sensing test platform was successfully built, which mainly includes three parts: a universal material tester (CMT model E42, MTS) that continuously and stably applies pressure to the sensor, an electrochemical workstation (ET 2000) for real-time online recording of current signals and a computer with related control software. During the sensing performance test, unless otherwise specified, the compression speed of the universal material tester was set to 1 mm/min, and the test voltage of the electrochemical workstation was set to 0.2 V. The current-voltage curve (I-V) of the sensor was measured using an electrochemical workstation (ET 2000) in potentiodynamic scanning mode (-1 V-1 V).

Joule heating performance. The Joule heating behavior of the composite fabric (size:1.5 cm × 2 cm) was studied by applying a certain voltage to the sample using a DC power supply (DPM8608) and simultaneously recording the change in the surface temperature of the fabric with an infrared thermal imager (FOTRIC 688#L25).

Photothermal conversion performance. The photothermal conversion properties of the composite fabrics (size:1.5 cm ×2 cm) were characterized using a xenon light source (CEL-HXF300) and a corresponding radiometer (CEL-FZ-A). At the same time, an infrared thermal imager (FOTRIC 688#L25) was used to record the surface temperature of the composite fabric.

Antibacterial properties. The antibacterial properties of textiles were determined by the oscillation method according to the standard GB/T 20944.3-2008. The antibacterial properties of the composite fabrics were evaluated by culturing in the coexistence of composite fabric ($AgNPs_{-6}$@$MNWF_{-5}$, $AuNPs_{-6}$@$MNWF_{-5}$, MNWF) and bacterial solution (E. coli and S. aureus), and NWF and $AuNPs_{-6}$@NWF were also tested as control and comparison samples, respectively. Among them, AgNPs@NWF was obtained by reducing $AgNO_3$ on NWF using ascorbic acid, where the loading of AgNPs was the same as that in $AgNPs_{-6}$@MNWF. The whole antibacterial experiment was carried out on an ultra-clean test bench. First, the composite textile is cut into 2 cm×1.5 cm squares and treated with UV disinfection. Subsequently, the bacterial solution was diluted with PBS to the initial concentration of bacterial strains was approximately 10^4 colony forming units (CFU)/mL. The composite fabric was mixed with 10 mL of bacterial solution, sealed in a 50 mL round bottom centrifuge tube, and then placed in a thermostatic shaker (SKY-100). The thermostatic oscillator was operated at 25 °C and 150 rpm for 24 hours. Then, 100 μL of the diluted mixture was pipetted and spread on a nutrient agar medium, incubated at 37°C for 18 hours until bacterial colonies became visible and countable, colony counting and photographing.

The percentage decrease of the bacterial solution concentration in the experimental group was calculated by comparing it with the control group. That is, the antibacterial performance of the composite fabric was obtained. The bacterial reduction rate was calculated using the following equation: [1]

$$R = \frac{(N_c - N_m)}{N_c} \times 100$$

Where N_c and N_m represent the number of colonies in the NWF (control fabric) and composite fabric, respectively.

Figures

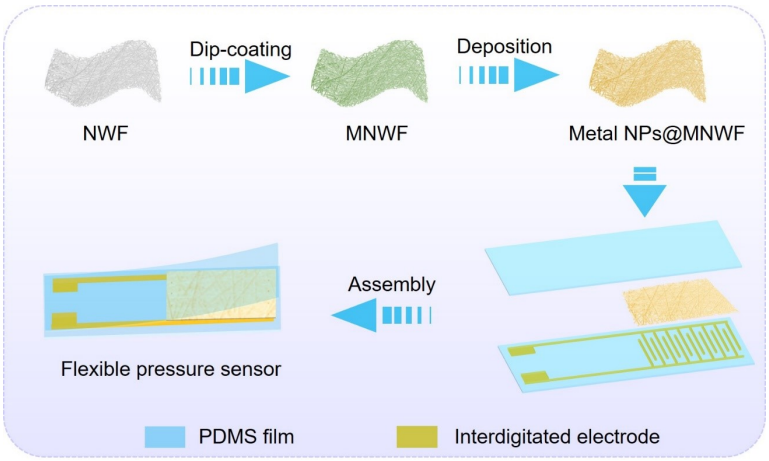

Scheme S1. Schematic diagram of the assembly process of the flexible pressure sensor.

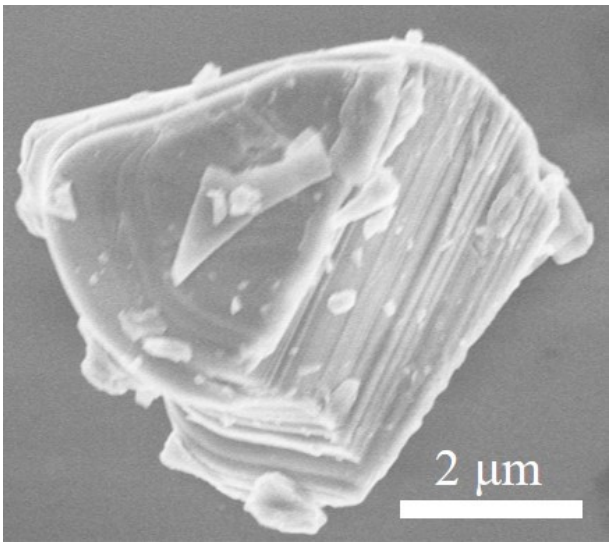

Fig. S1. SEM image of Ti_3AlC_2.

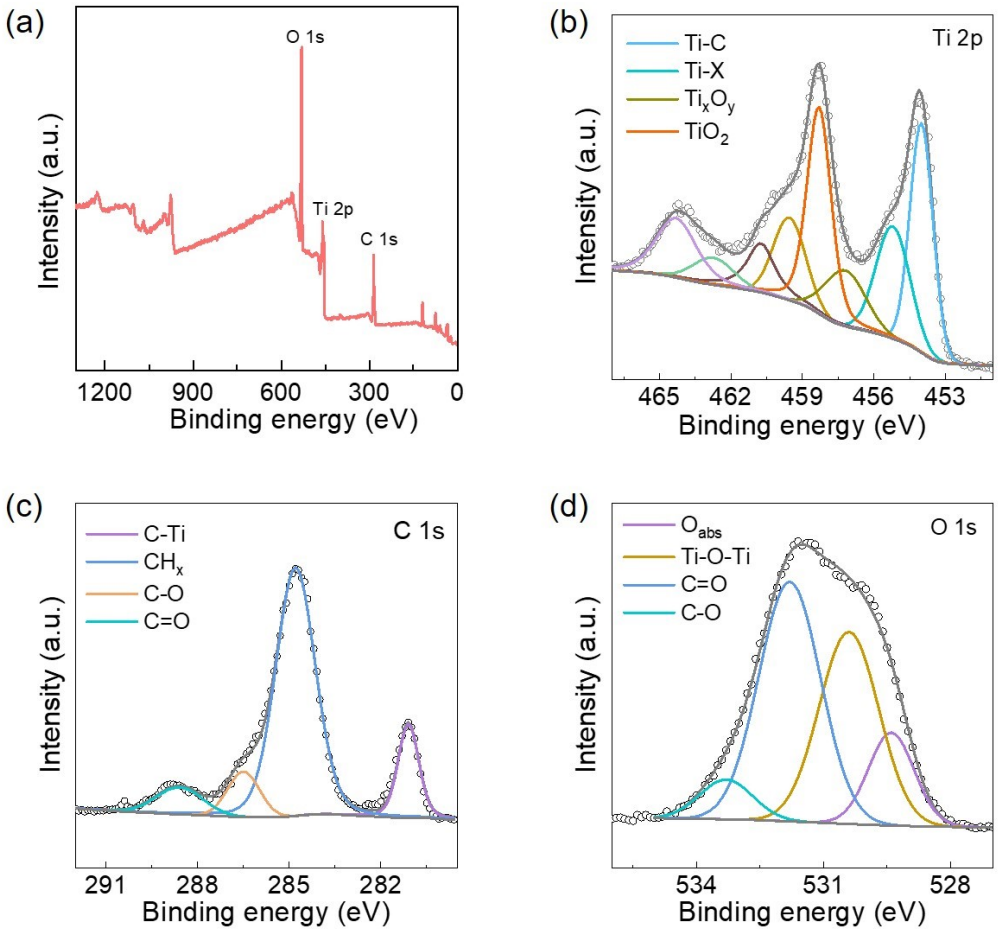

Fig. S2. (a) XPS spectrum of Ti_3AlC_2. High-resolution XPS spectrum of (b) Ti 2p, (c) C1s, (d) O1s.

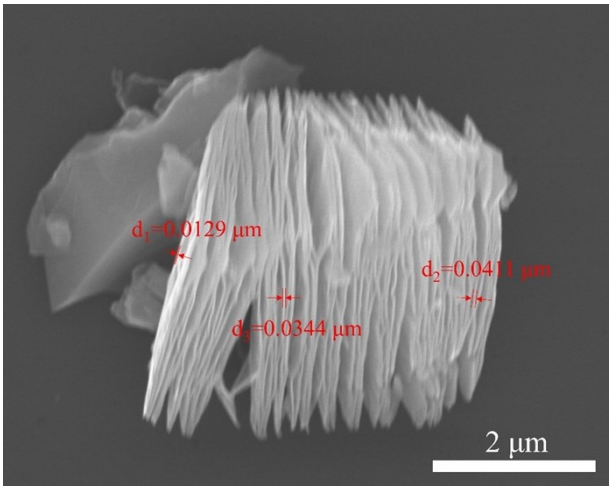

Fig. S3. SEM image of m-$Ti_3C_2T_x$.

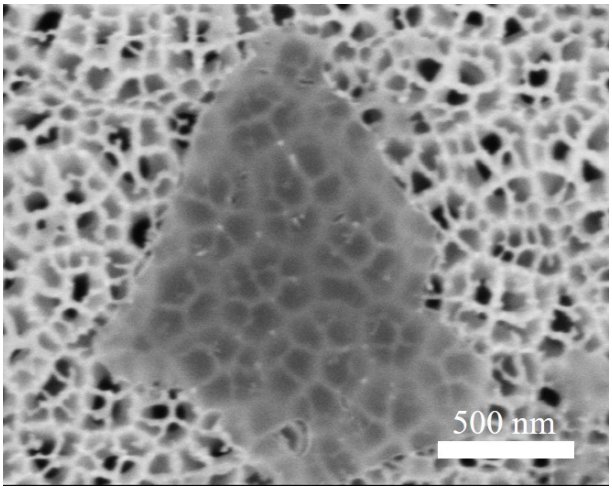

Fig. S4. SEM image of s-$Ti_3C_2T_x$ nanosheet.

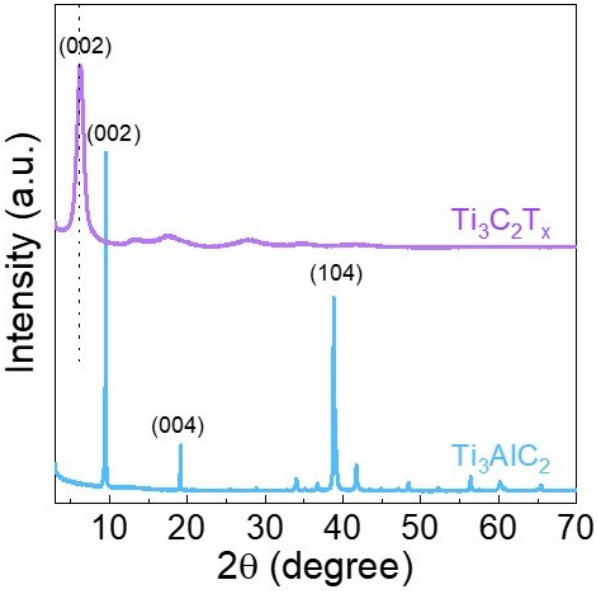

Fig. S5. XRD Pattern of Ti_3AlC_2 and s-$Ti_3C_2T_x$.

The successful synthesis of $Ti_3C_2T_x$ was confirmed by the disappearance of the (104) plane and the blue shift of the (002) plane in the XRD pattern.

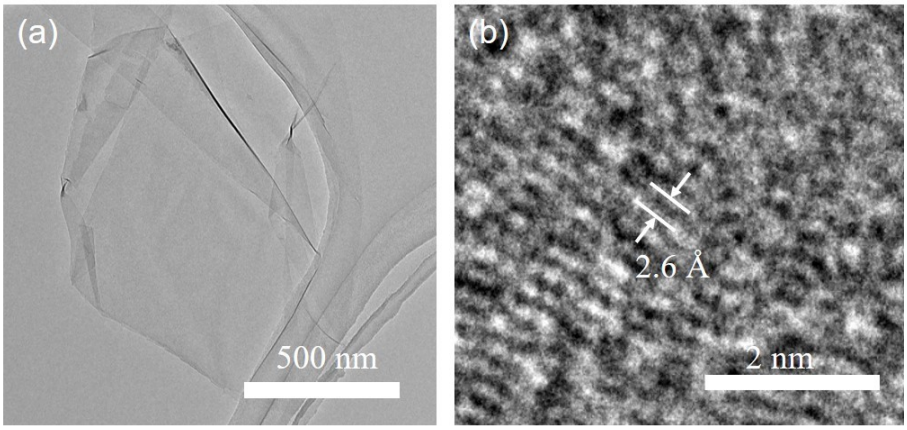

Fig. S6. (a) TEM image of s-$Ti_3C_2T_x$ nanosheet. (b) HR-TEM image of a typical s-$Ti_3C_2T_x$ nanosheet.

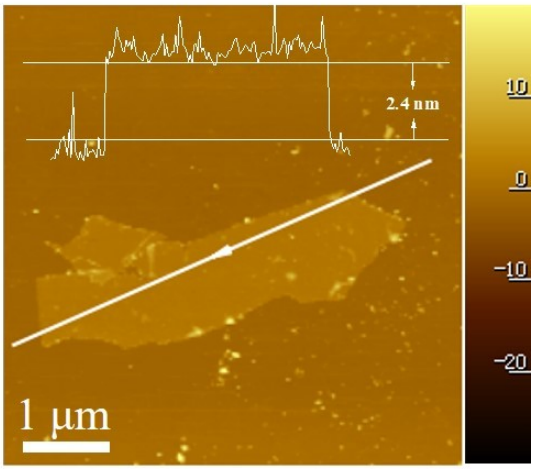

Fig. S7. AFM image of s-$Ti_3C_2T_x$ nanosheet and the corresponding height value.

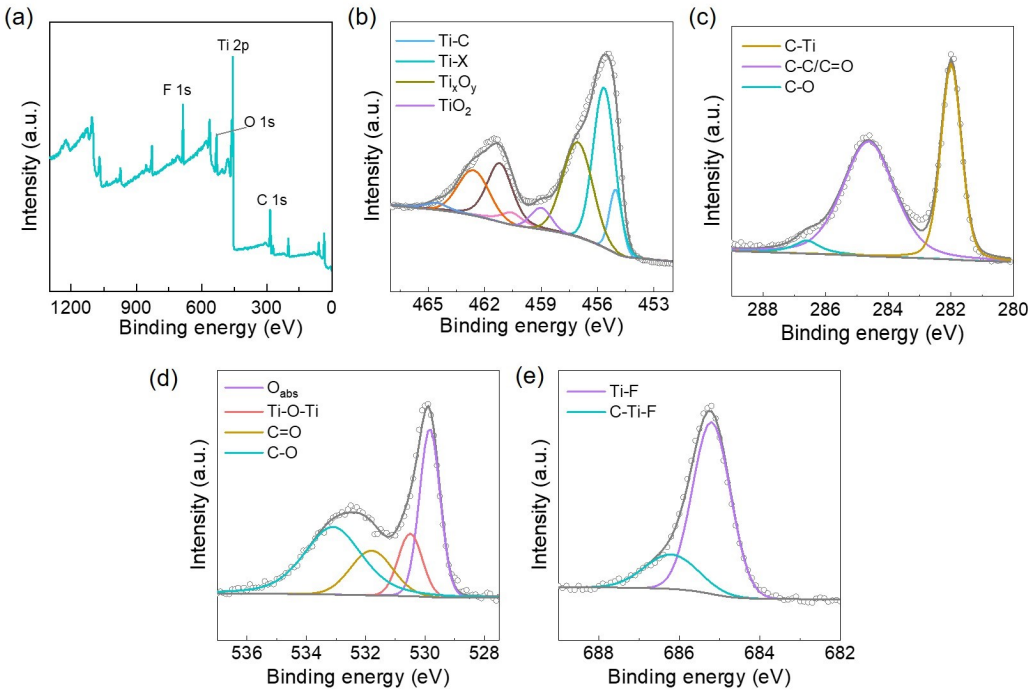

Fig. S8. (a) XPS spectrum of s-$Ti_3C_2T_x$. High resolution XPS spectrum of (b) Ti 2p, (c) C 1s, (d) O 1s, (e) F 1s.

Fig. S9. Tyndall phenomenon of MXene aqueous solution.

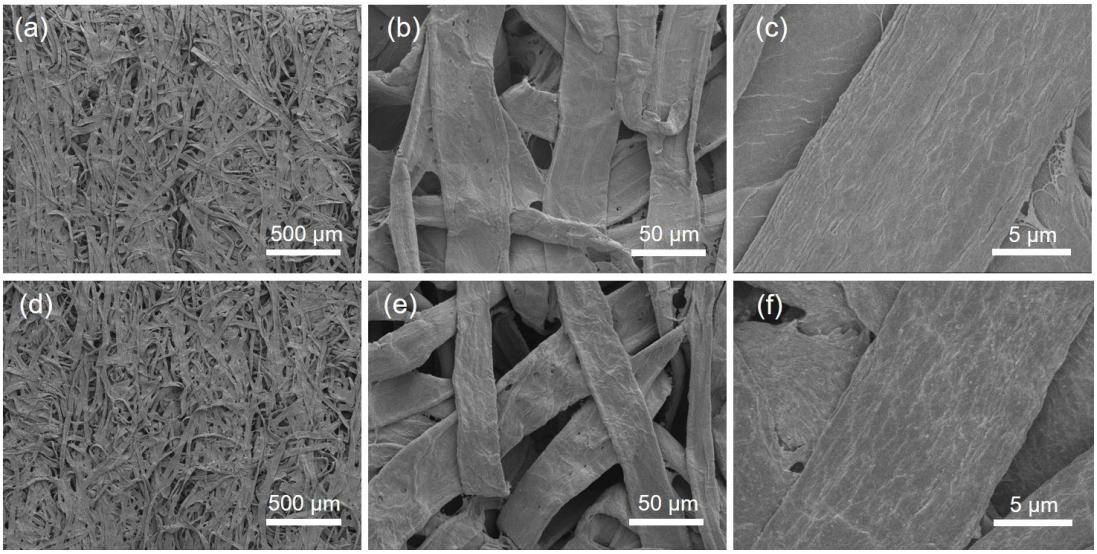

Fig. S10. SEM image of NWF (a-c) and MNWF (d-e) at different magnifications.

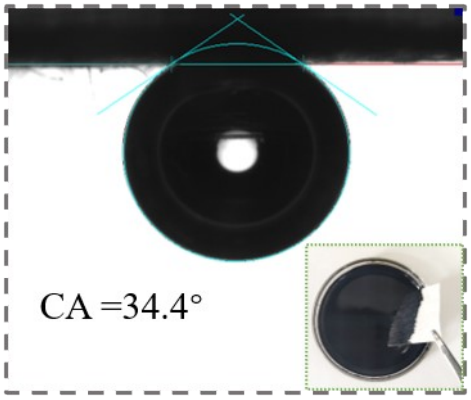

Fig. S11. Contact angle of NWF (inset: rapid penetration of NWF by MXene aqueous solution).

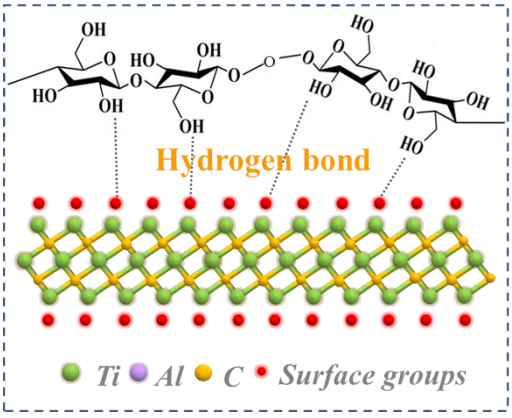

Fig. S12. Schematic of hydrogen bonding between MXene nanosheets and cellulose.

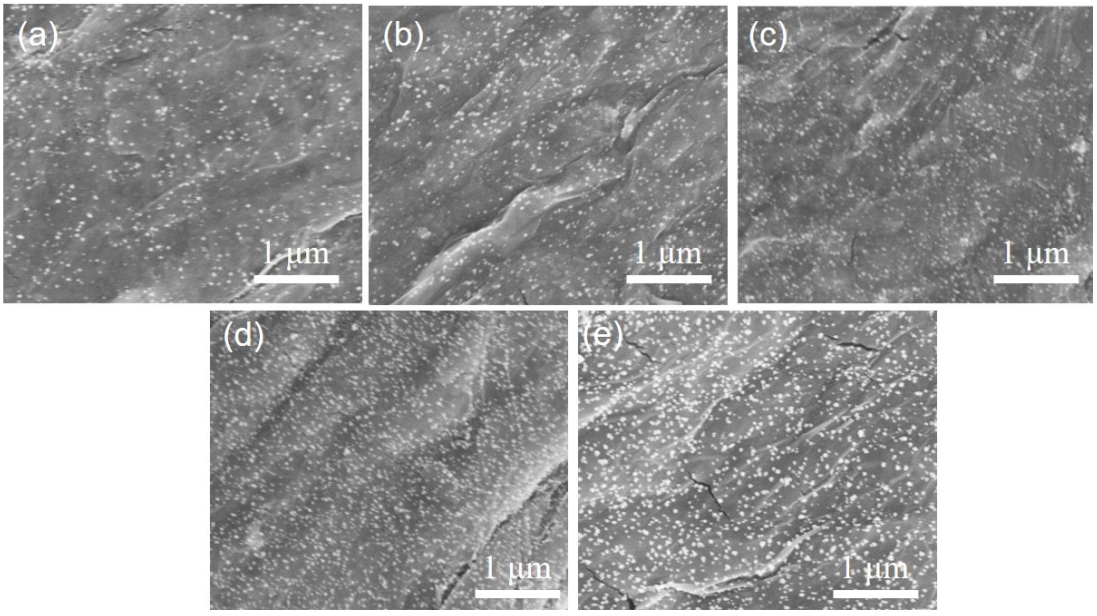

Fig. S13. Typical SEM images of spontaneous in situ growth of AuNPs on MNWF surface with different metal contents (a) 2 wt%, (b) 4 wt%, (c) 6 wt%, (d) 8 wt%, (e) 10 wt%.

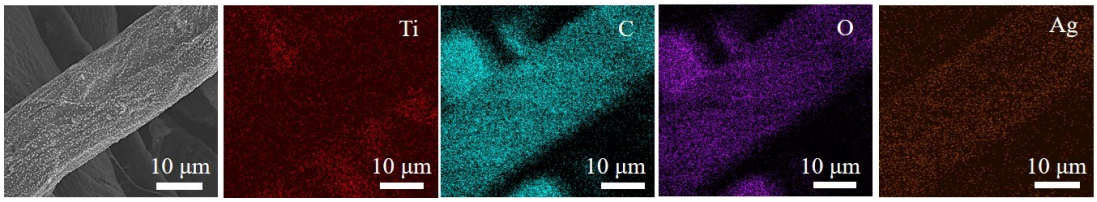

Fig. S14. EDS mapping of AgNPs$_{-6}$@MNWF$_{-5}$.

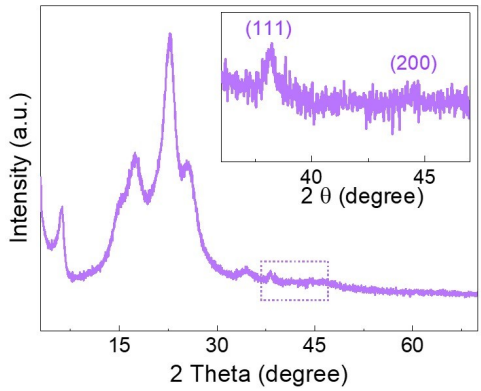

Fig. S15. XRD pattern of AgNPs$_{-6}$@MNWF$_{-5}$.

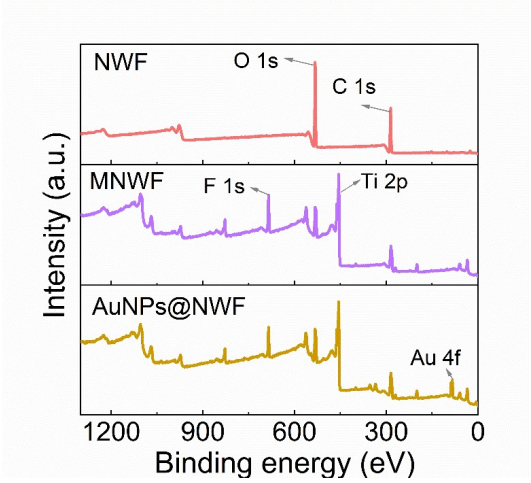

Fig. S16. XPS survey spectra of NWF, MNWF, and AuNPs@MNWF.

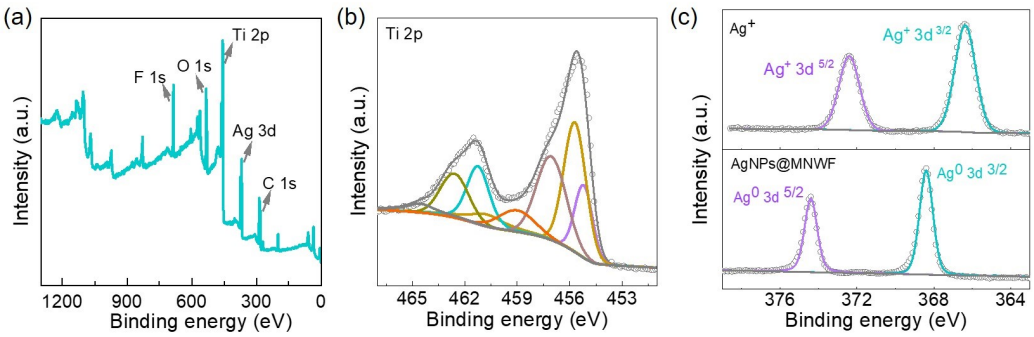

Fig. S17. (a) XPS spectrum of AgNPs$_{-6}$@MNWF$_{-5}$. High resolution XPS spectrum of (b) Ti 2p, (c) Ag 3d.

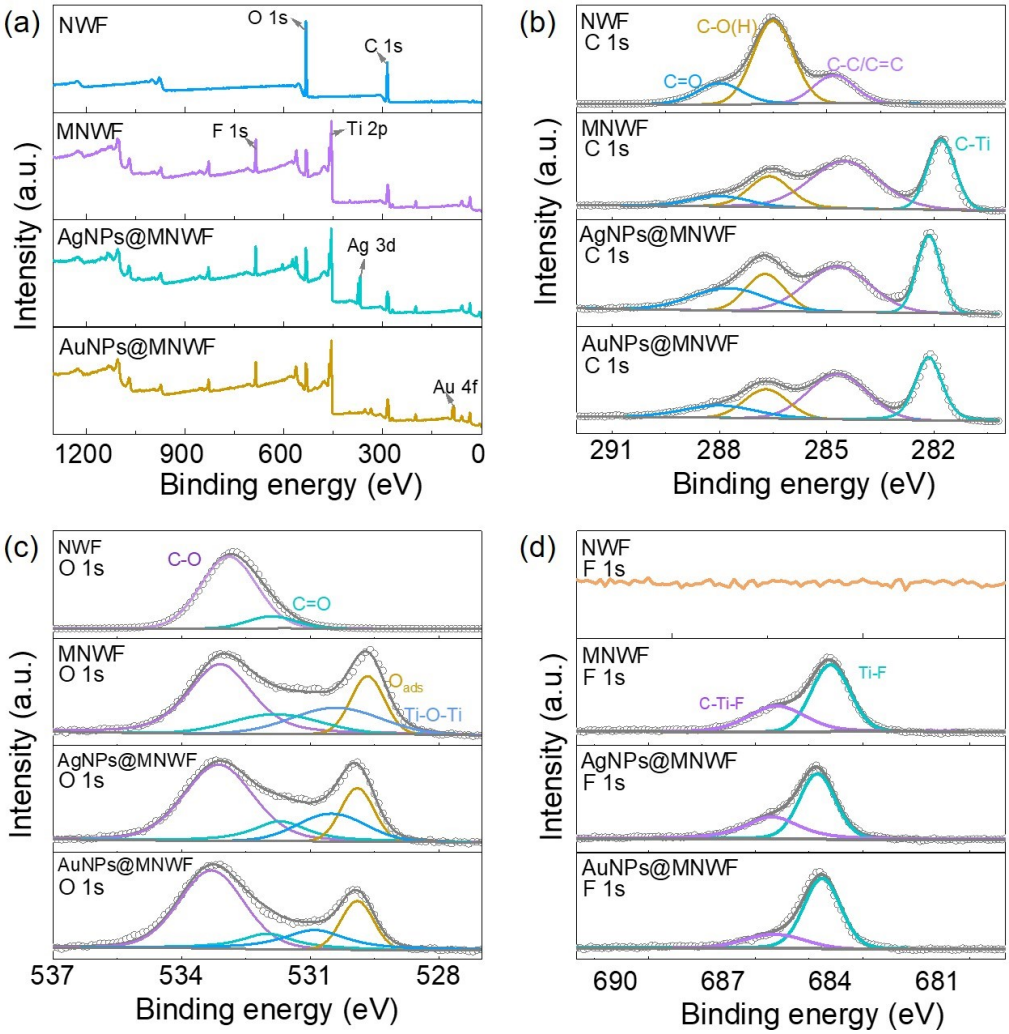

Fig. S18. (a) XPS spectrum of NWF, MNWF, AgNPs$_{-6}$@MNWF$_{-5}$, and AuNPs$_{-6}$@MNWF$_{-5}$. High resolution XPS spectrum of (b) C 1s, (C) O 1s, (d) F 1s.

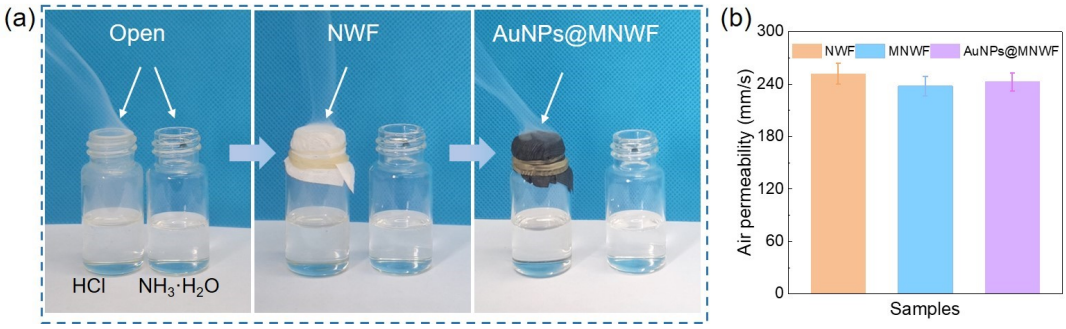

Fig. S19. (a) Two glass bottles containing HCl and $NH_3{\cdot}H_2O$, covered with NWF and AuNPs$_{-6}$@MNWF$_{-5}$, respectively. (b) The corresponding air permeability of NWF, MNWF$_{-5}$ and AuNPs$_{-6}$@MNWF$_{-5}$, respectively.

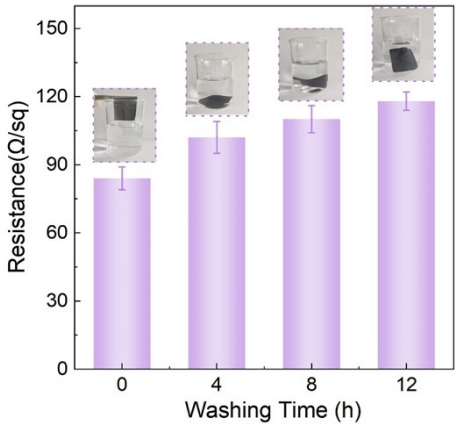

Fig. S20. Change of relative resistance rate with washing time. The inset is the digital photos of the AuNPs$_{-6}$@MNWF$_{-5}$ corresponding to different washing times.

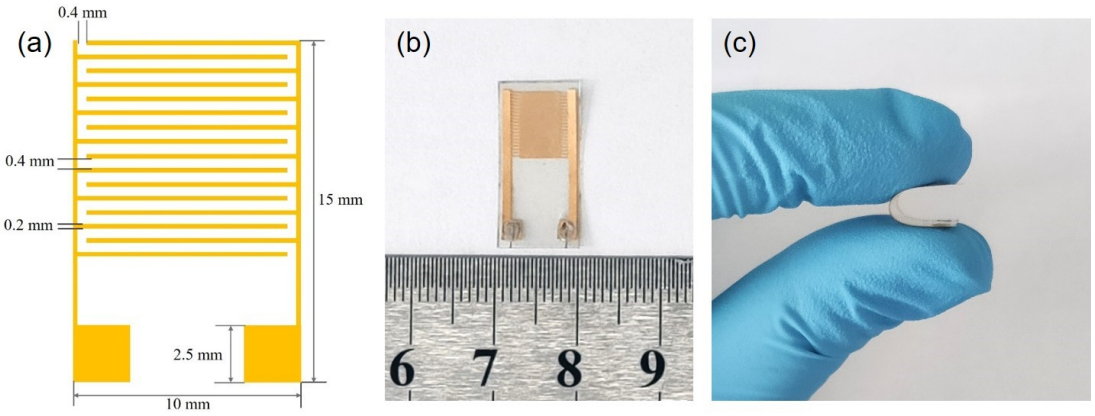

Fig. S21. (a) Specific dimensions of PI-IDE. (b) Photograph of PI-IDE. (c) PI-IDE bent by hand.

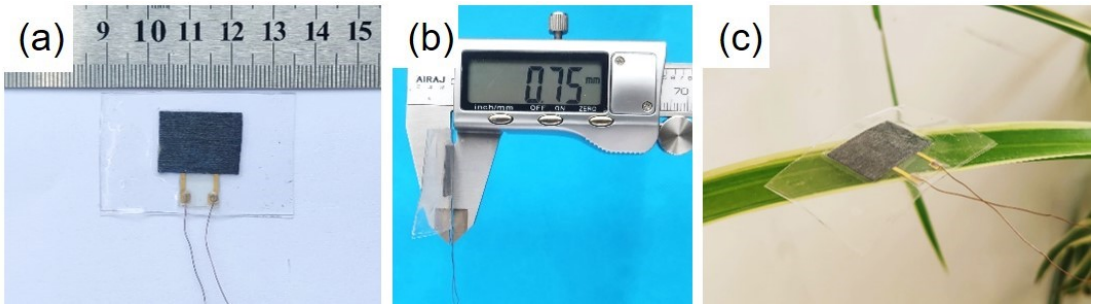

Fig. S22. (a) Photograph of flexible pressure sensor. (b) Thickness of the flexible pressure sensor. (c) The device is lightweight and easily supported by a leaf.

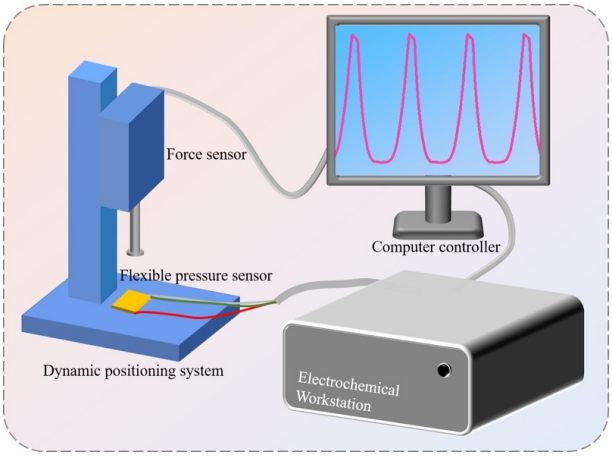

Fig. S23. Schematic illustration of the pressure-sensing experimental setup.

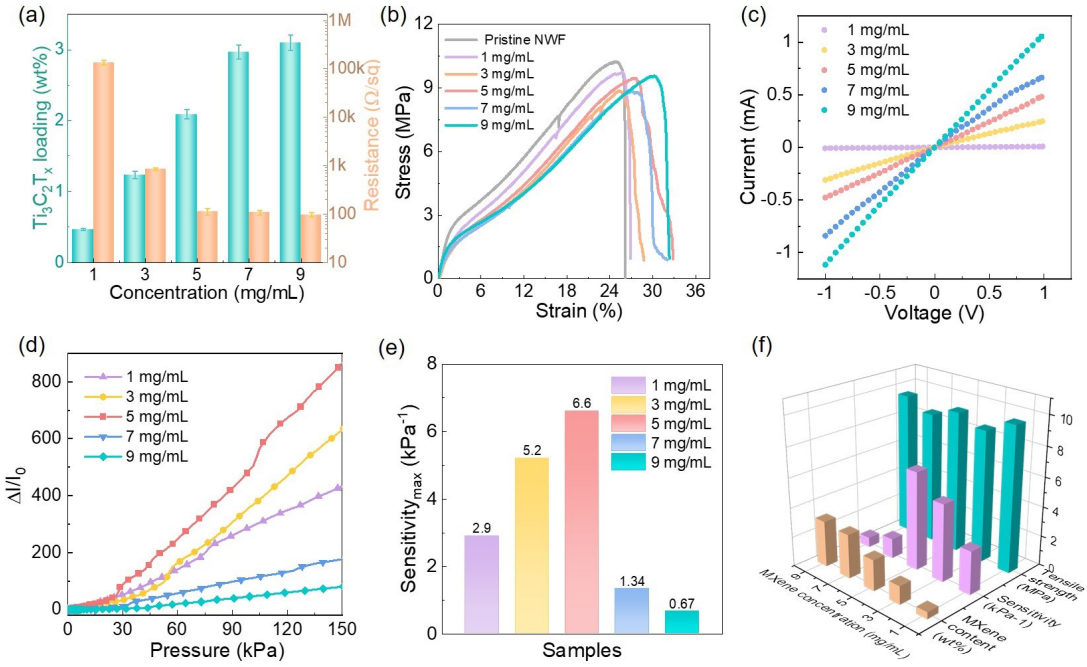

Fig. S24. (a) $Ti_3C_2T_x$ content and corresponding sheet resistance. (b) Stress-strain curves of MNWF. (c) I-V curves of MNWF-based pressure sensors. (d) Sensitivity curve of MNWF-based sensors. (e) Maximum sensitivity. (f) The comparison of tensile strength, sensitivity, and MXene content of MNWF with different MXene concentrations.

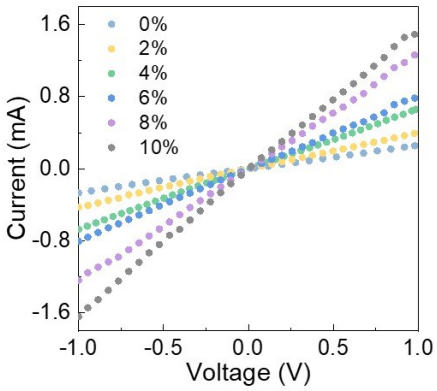

Fig. S25. I-V curves AuNPs@MNWF$_{-5}$ -based flexible pressure sensors with different AuNPs contents.

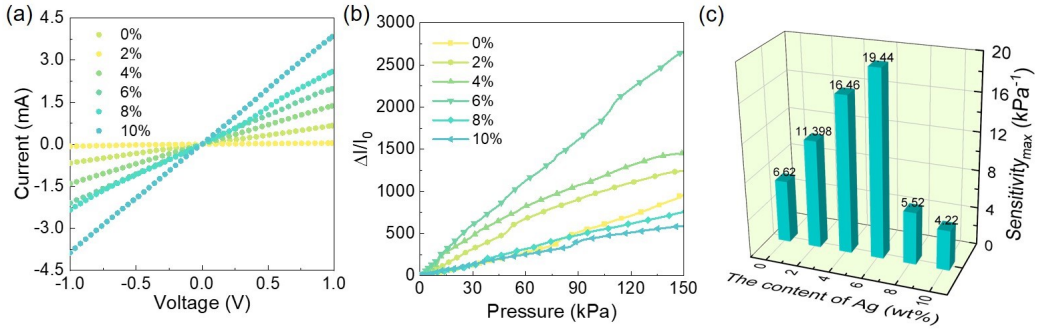

Fig. S26. (a) I-V curves, (b) Sensitivity, and (c) Maximum sensitivity of AgNP@MNWF$_{-5}$ -based flexible pressure sensors with different AgNPs contents.

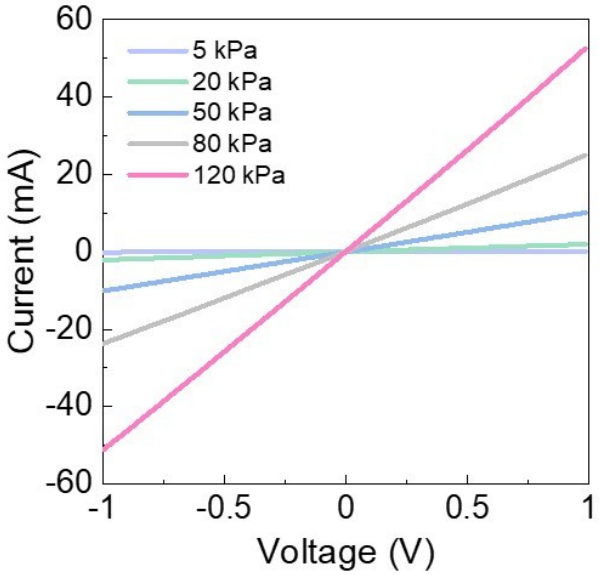

Fig. S27. I-V curves of AuNPs$_{-6}$@MNWF$_{-5}$ flexible pressure sensor under a series of static pressures (5-120 kPa).

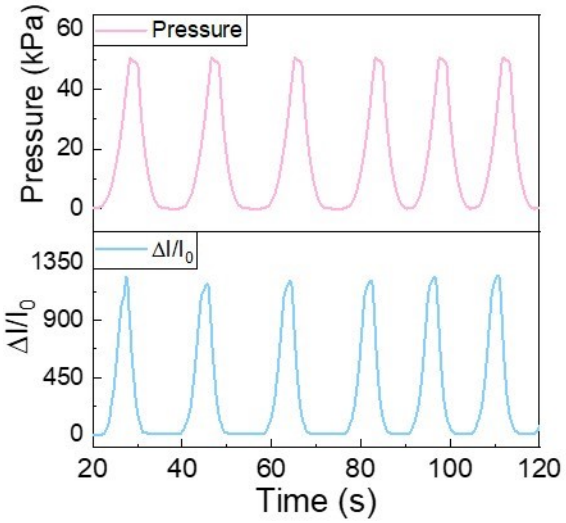

Fig. S28. Correspondence between input pressure signal and output current signal.

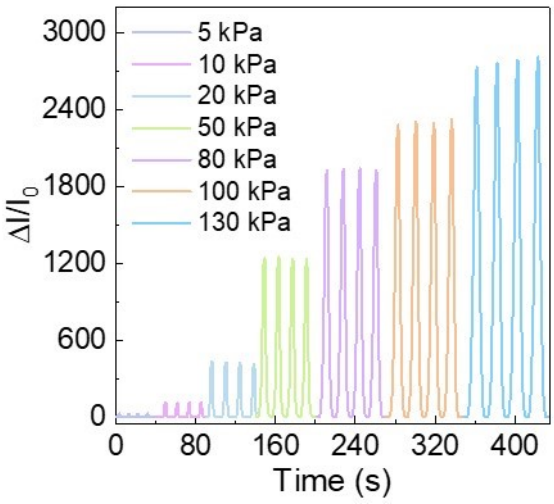

Fig. S29. $\Delta I/I_0$ curves at different pressures (5–130 kPa).

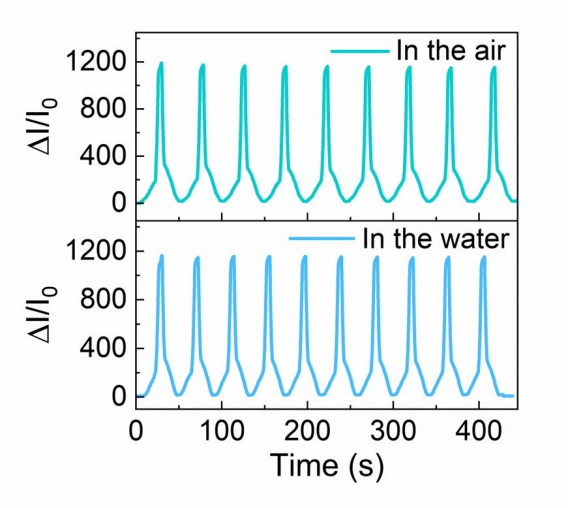

Fig. S30. The current response of the sensor when a pressure of 50 kPa is applied to the sensor in air and water, respectively.

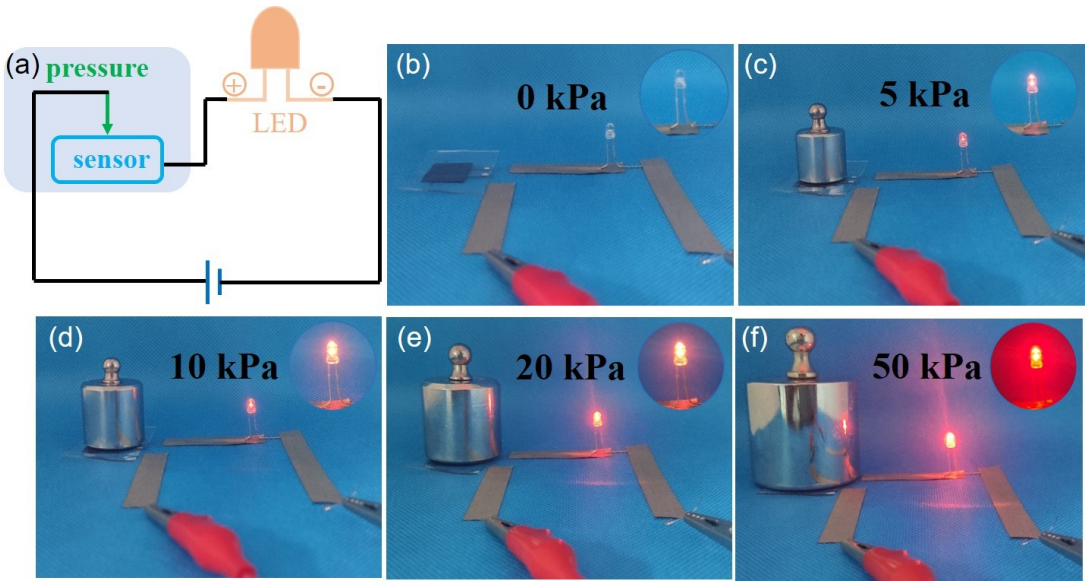

Fig. S31. (a) Schematic diagram of the AuNPs$_{-6}$@MNWF$_{-5}$ pressure sensor and LED series circuit. (b-f) LED brightness in response to different weights (0–50 g) placed on the pressure sensor.

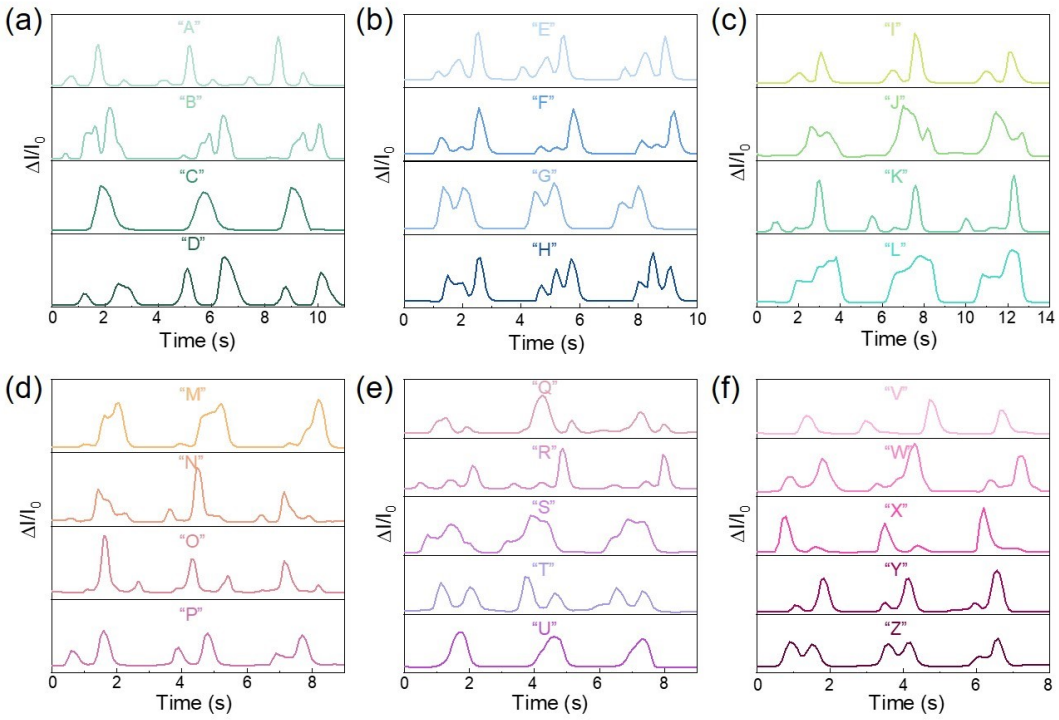

Fig. S32. Signal curves corresponding to 26 letters written on the sensor surface (a) A-D, (b) E-H, (c) I-L, (d) M-P, (e) Q-U, (f) V-Z.

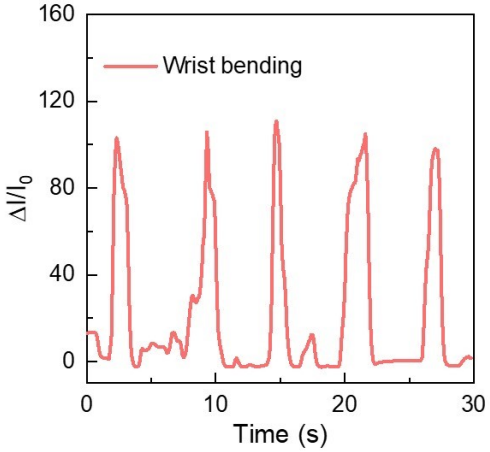

Fig. S33. $\Delta I/I_0$ signal generated by wrist bending.

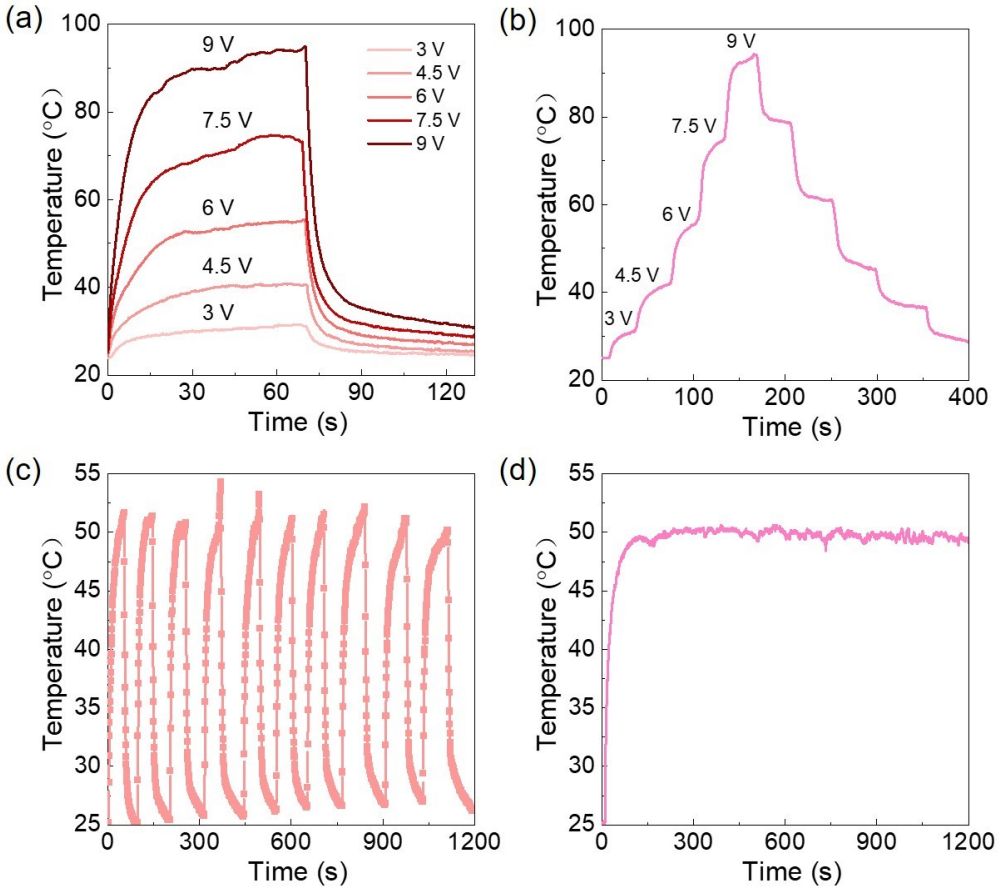

Fig. S34. (a) Joule heating performance of $MNWF_{-5}$ at different voltages (3-9V). (b) Tailored surface temperatures of the $MNWF_{-5}$ at a stepwise voltage increase from 3 to 9V. (c) Temperature−time curve of $MNWF_{-5}$ under a 6 V input voltage for ten cycles. (d) Long-term Joule heating performances at a constant voltage of 5 V.

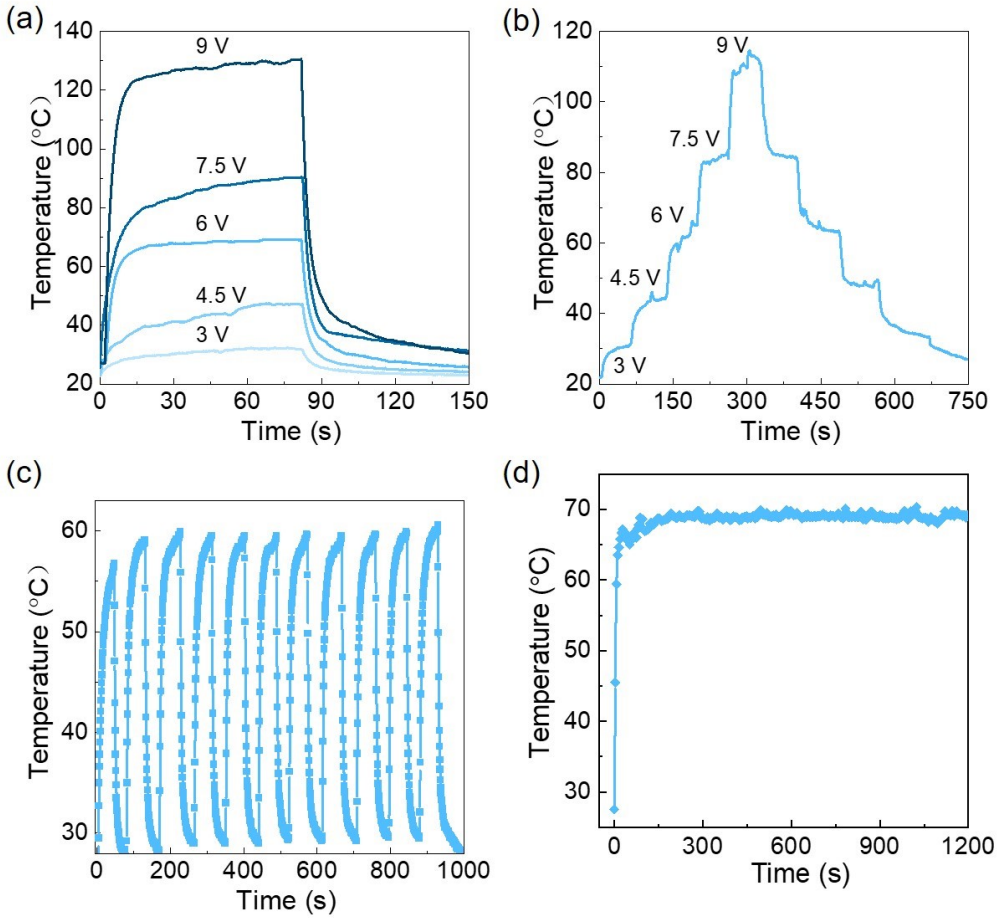

Fig. S35. (a) Joule heating performance of AuNPs$_{-6}$@MNWF$_{-5}$ at different voltages (3-9V). (b) Tailored surface temperatures of the AuNPs$_{-6}$@MNWF$_{-5}$ at a stepwise voltage increase from 3 to 9 V. (c) Temperature−time curve of AuNPs$_{-6}$@MNWF$_{-5}$under a 6 V input voltage for ten cycles. (d) Long-term Joule heating performances at a constant voltage of 6V.

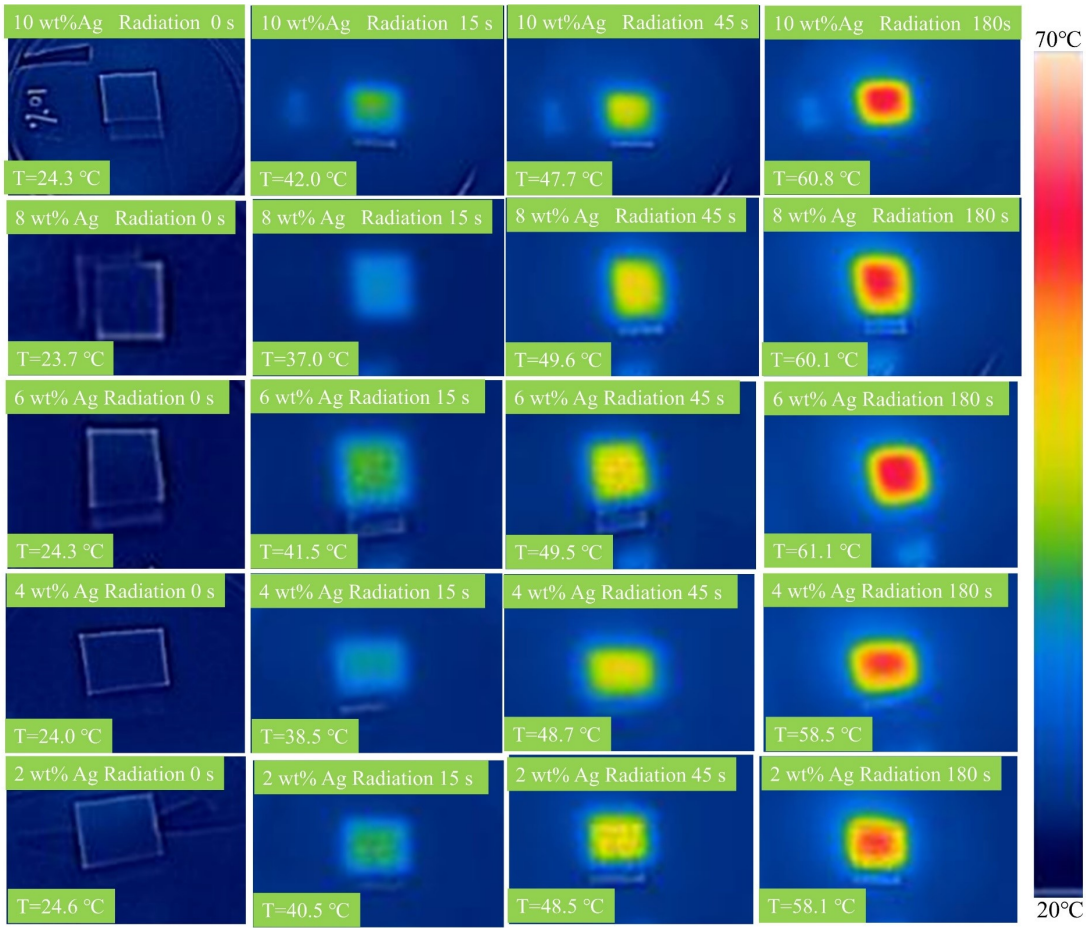

Fig. S36. IR images of AgNPs@MNWF$_{-5}$ with different AgNPs contents under 100 mW/cm^2 power irradiation at different times.

Fig. S37. Photographs of AgNPs$_{-6}$@MNWF$_{-5}$ wrapped on a pen and the corresponding IR image.

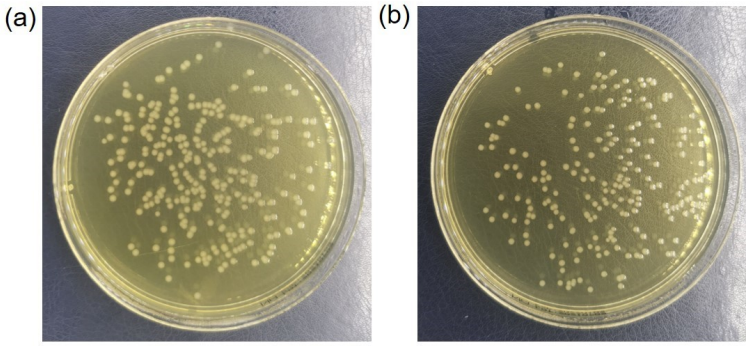

Fig. S38. (a) Photograph of agar plates onto which E. coli bacterial cells were recultivated after treatment with (a) NWF and (b) $AgNPs_{-6}$@NWF.

Tables

Table S1. XPS Fitting Results of Ti_3AlC_2.

Element	Component name	BE（eV）	Area	FWHM（eV）
Ti 2p	Ti−C	454 (459.5)	23433.51 (11716.75)	1.15 (1.59)
	Ti−X	455.2 (460.7)	16911.54 (8455.772)	1.68 (1.4)
	Ti_xO_y	457.2 (462.7)	9958.115 (4979.058)	2 (2)
	TiO_2	458.3 (464.3)	25214.43 (12607.21)	1.2 (2)
C 1s	C-Ti	281.1	7336.625	0.8
	CH_x	284.8	35811.18	1.53
	C-O	286.5	4909.511	1.24
	C=O	288.6	4226.154	1.79
O 1s	O_{ads}	529.4	21009.44	1.27
	Ti-O-Ti	530.4	55760.99	1.66
	C=O	531.8	71977.2	1.71
	C-O	533.3	10232.23	1.47

Table S2. XPS Fitting Results of $Ti_3C_2T_x$.

Element	Component name	BE（eV）	Area	FWHM（eV）
Ti 2p	Ti−C	455.0 (460.58)	18800.42 (9400.211)	0.8 (1.4)
	Ti−X	455.6 (461.2)	79692.88 (39846.44）	1.35 (1.6)
	Ti_xO_y	457.1 (462.6)	65078.54 (32539.27)	1.87(1.95)
	TiO_2	459 (464.5)	10075.1 (5037.552)	1.27 (1.4)
C 1s	C–C/C=C	284.63	38010.71	1.94
	C–O(H)	286.6	2857.369	1
	C-Ti	281.9	24850.56	0.77
O 1s	O_{ads}	529.8	17830.56	0.82
	Ti−O−Ti	530.5	7511.59	0.95
	C=O	531.8	9414.66	1.66
	C-O	533.1	23172.9	2.3
F 1s	Ti–F	685.2	37478.06	1.1
	C-Ti-F	686.2	10600.2	1.56

Table S3. XPS fitting results of Ti 2p.

Samples	Component name	BE（eV）	Area	FWHM（eV）
NWF	-	-	-	-
MNWF	Ti−C	454.9 (460.4)	22740.47 (22739.97)	0.81 (2)
	Ti−X	455.6 (461.1)	95918.8 (47959.4)	1.86 (1.67)
	Ti_xO_y	457.2 (462.7)	35844.6 (17922.3)	2.01 (1.92)
	TiO_2	459.0 (464.5)	3419.556 (1709.78)	0.87 (0.5)
AuNPs@MNWF	Ti−C	455.0 (460.5)	15000 (7500)	1 (2)
	Ti−X	455.5 (461.1)	75952.47 (37976.23)	1.55 (1.86)
	Ti_xO_y	457.1 (462.6)	62111.55 (31055.78)	2.03 (2.13)
	TiO_2	459.0 (464.5)	8148.174 (4074.087)	1.05 (1.39）
AgNPs@MNWF	Ti−C	455.2 (460.7)	22611.72 (11305.86)	1.2 (2.4)
	Ti−X	455.7 (461.2)	50412.27 (25206.13)	1.5 (1.5)
	Ti_xO_y	457.1 (462.6)	43362.84 (21681.42)	2 (1.9)
	TiO_2	459 (464.5)	13596.88 (6798.44)	2.4 (2)

Table S4. Standard electrode potential

Electrode reaction	Potential /V
$Ti^{3+} + e^- = Ti^{2+}$	-0.37
$Ti^{2+} + 2e^- = Ti$	-1.63
$Ag^+ + e^- = Ag$	+0.799
$AuCl^-_4 + 3e^- = Au + 4Cl^-$	+1.002

Table S5. XPS fitting results of Au 4f and Ag 3d.

Element	Samples	Component name	BE（eV）	Area	FWHM（eV）
Au 4f	$HAuCl_4$	Au 4f $^{5/2}$	86.8	3662.318	1.32
		Au 4f $^{7/2}$	83.2	4382.466	1.34
	AuNPs@MNWF	Au 4f $^{5/2}$	87.9	21598.13	0.82
		Au 4f $^{7/2}$	84.2	24395.92	0.84
Ag 3d	$AgNO_3$	Ag 3d$^{5/2}$	366.4	41614.17	1.27
		Ag 3d$^{3/2}$	372.4	28176.63	1.25
	AgNPs@MNWF	Ag 3d$^{5/2}$	368.4	38149.4	0.82
		Ag 3d$^{3/2}$	374.4	26875.35	0.77

Table S6. XPS fitting results of C1s.

Samples	Component name	BE（eV）	Area	FWHM（eV）
NWF	C–C/C=C	284.8	27949.75	1.5
	C–O(H)	286.5	81718.45	1.5
	C=O	288	26028.37	1.5
MNWF	C–C/C=C	284.8	40136.68	2.3
	C–O(H)	286.6	15690.99	1.4
	C=O	288	6925.515	1.9
	C-Ti	281.8	6925.515	0.9
AuNPs@MNWF	C–C/C=C	284.7	32535.1	2.0
	C–O(H)	286.7	15406.34	1.4
	C=O	288	12082.22	2.4
	C-Ti	282	23730.6	0.9
AgNPs@MNWF	C–C/C=C	284.7	24845.73	2.15
	C–O(H)	286.7	11897.52	1.29
	C=O	287.7	14221.52	2.47
	C-Ti	282.1	15441.66	0.78

Table S7. XPS fitting results of O1s.

Samples	Component name	BE（eV）	Area	FWHM（eV）
NWF	C–O	532.9	200976.3	1.5
	C=O	531.9	27729.59	1.3
MNWF	C–O	533.1	45242.02	1.74
	C=O	531.8	14853.57	2.49
	O_{ads}	529.7	16427.39	0.92
	Ti−O−Ti	530.4	19497.77	2.41
AuNPs@MNWF	C–O	533.1	52922.67	1.9
	C=O	531.7	13416.05	1.48
	O_{ads}	529.9	15834.86	0.9
	Ti−O−Ti	530.5	16857.57	1.85
AgNPs@MNWF	C–O	533.3	47765.55	1.77
	C=O	532.0	10983.83	1.48
	O_{ads}	529.9	14126.52	0.89
	Ti−O−Ti	530.9	15917.92	1.78

Table S8. XPS fitting results of F1s.

Samples	Component name	BE（eV）	Area	FWHM（eV）
NWF	-	-	-	-
MNWF	Ti–F	684.9	42724.97	1.27
	C-Ti-F	686.4	27099.4	1.88
AuNPs@MNWF	Ti–F	685.1	40168.98	1.21
	C-Ti-F	686.5	11892.92	1.95
AgNPs@MNWF	Ti–F	685.3	32977.66	1.19
	C-Ti-F	686.5	20671.84	1.78

Table S9. Sensing performance comparison of piezoresistive fabric-based pressure sensors.

Fabric-based pressure sensor	S_{max}（kPa^{-1}）	Sensing range (kPa)	Response/recovery time (ms)	Durability (cycles)	Ref.
MXene/Cotton woven fabric	7.67	0-2	35/35	2000	[2]
Si-MAP	5.78	0-20	40/30	5000	[3]
MXene/cotton fabric	5.3	0-160	50/20	1000	[4]
PEDOT:PSS/cotton-based nonwoven fabric	8.59	0.2-400	22/37	10000	[5]
GN/cotton fabric	1.08	0-6.8	60/60	3000	[6]
MXene/textile	12.095	0-40	26/50	5600	[7]
MXene/CNC/ TPU nonwoven fabrics	0.208	0-100	60/75	1000	[8]
MXene/scuba knit	23.7	0-5	71.5/18	20000	[9]
TiO_2-ODI/PEDOT:PSS/cotton fabric	0.85	0-50	158/157	1000	[10]
Phosphorene-AuNCs/ nylon thread	0.372	0-3.5	24/32	4000	[11]
AuNPs@MNWF	24.5	0-150	40/60	6000	This work

References

1. X. Liu, X. Jin, L. Li, J. Wang, Y. Yang, Y. Cao and W. Wang, *J. Mater. Chem. A*, 2020, **8**,

12526-12538.
2. R. Liu, J. Li, M. Li, Q. Zhang, G. Shi, Y. Li, C. Hou and H. Wang, *ACS Appl. Mater. Interfaces*, 2020, **12**, 46446-46454.
3. C. Ma, Q. Yuan, H. Du, M.-G. Ma, C. Si and P. Wan, *ACS Appl. Mater. Interfaces*, 2020, **12**, 34226-34234.
4. Y. Zheng, R. Yin, Y. Zhao, H. Liu, D. Zhang, X. Shi, B. Zhang, C. Liu and C. Shen, *Chem. Eng. J.*, 2021, **420**, 127720.
5. Z. Song, W. Li, H. Kong, M. Chen, Y. Bao, N. Wang, W. Wang, Z. Liu, Y. Ma, Y. He, Z. Kang and L. Niu, *Chemical Engineering Journal*, 2022, **444**.
6. Y. Zhao, L. Liu, Z. Li, F. Wang, X. Chen, J. Liu, C. Song and J. Yao, *J. Mater. Chem. C*, 2021, **9**, 12605-12614.
7. T. Li, L. Chen, X. Yang, X. Chen, Z. Zhang, T. Zhao, X. Li and J. Zhang, *J. Mater. Chem. C*, 2019, **7**, 1022-1027.
8. Q. Li, R. Yin, D. Zhang, H. Liu, X. Chen, Y. Zheng, Z. Guo, C. Liu and C. Shen, *J. Mater. Chem. A*, 2020, **8**, 21131-21141.
9. W. Fan, C. Li, W. Li and J. Yang, *Advanced Materials Interfaces*, 2022, DOI: 10.1002/admi.202102553.
10. L. Yang, J. Ma, W. Zhong, Q. Liu, M. Li, W. Wang, Y. Wu, Y. Wang, X. Liu and D. Wang, *J. Mater. Chem. C*, 2021, **9**, 5217-5226.
11. X. Weng, C. Zhang, C. Feng and H. Jiang, *Advanced Materials Interfaces*, 2022, DOI: 10.1002/admi.202102588.